

NEAT: Distilling 3D Wireframes from Neural Attraction Fields

Nan Xue¹ Bin Tan^{1,2} Yuxi Xiao^{1,3} Liang Dong⁴ Gui-Song Xia² Tianfu Wu^{5*} Yujun Shen¹
¹Ant Group ²Wuhan University ³Zhejiang University ⁴Google Inc. ⁵NC State University

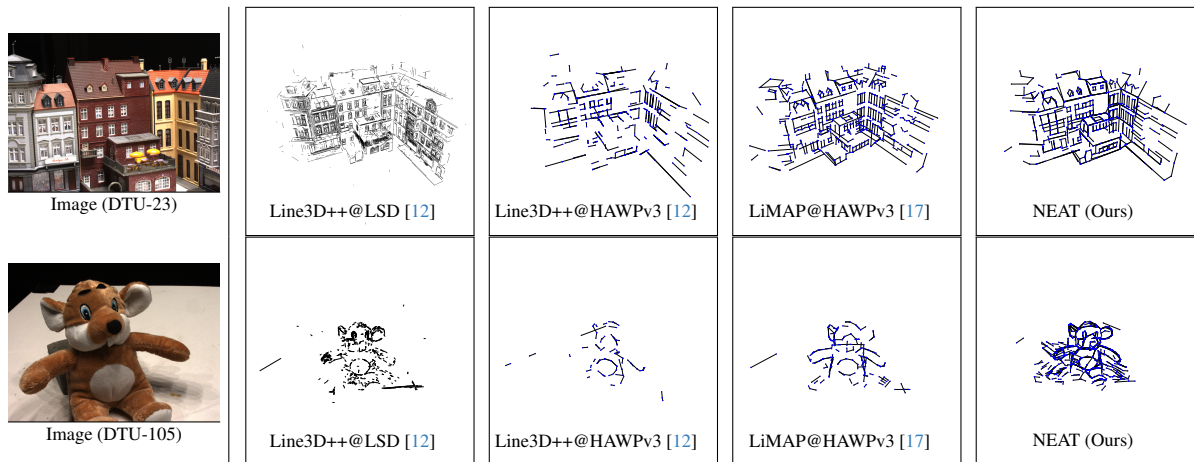


Figure 1. **Showcasing the evolution of 3D wireframe reconstruction:** The top reveals the transformative steps from a straight-line dominated urban landscape to an abstract wireframe, contrasting various methodologies. Below, the intricate transition from a curve-rich stuffed animal to its skeletal representation is depicted. While Line3D++ [12] and LiMAP [17] utilize line-matching techniques, our novel NEAT approach forgoes matching, resulting in superior reconstruction fidelity with our proposed rendering-distilling formulation.

Abstract

This paper studies the problem of structured 3D reconstruction using wireframes that consist of line segments and junctions, focusing on the computation of structured boundary geometries of scenes. Instead of leveraging matching-based solutions from 2D wireframes (or line segments) for 3D wireframe reconstruction as done in prior arts, we present NEAT, a **rendering-distilling** formulation using neural fields to represent 3D line segments with 2D observations, and bipartite matching for perceiving and distilling of a sparse set of 3D global junctions. The proposed NEAT enjoys the joint optimization of the neural fields and the global junctions from scratch, using view-dependent 2D observations without precomputed cross-view feature matching. Comprehensive experiments on the DTU and BlendedMVS datasets demonstrate our NEAT’s superiority over state-of-the-art alternatives for 3D wireframe reconstruction. Moreover, the distilled 3D global junctions by NEAT, are a better initialization than SfM points, for the recently-emerged 3D Gaussian Splatting for high-fidelity novel view synthesis using about 20 times fewer initial 3D points. Project page: <https://xuenan.net/neat>.

1. Introduction

In this paper, we explore the field of multi-view 3D reconstruction, drawing inspiration from the paradigm of the primal sketch proposed by D. Marr [19]. Our objective is to develop a concise yet precise representation of 3D scenes, derived from multi-view images with known camera poses. Specifically, our focus is on wireframe representations [44, 46, 51, 52], which define the boundary geometry of scene images through line segments and junctions as the 2D wireframe representation. We dedicate our efforts to advancing the reconstruction of 3D wireframes based on their 2D counterparts detected in multi-view images, as shown in Fig. 1 and Fig. 2.

The challenge of *multi-view 3D wireframe reconstruction* has been previously explored within the realm of line-based 3D reconstruction [12, 17, 39], primarily following the feature triangulation pipelines [29], which heavily rely on the accuracy of multi-view feature correspondences. Various methods have been developed to enhance this accuracy [23, 24, 39]. However, a significant challenge arises from view-dependent occlusions of line features: when projecting a 3D line segment onto 2D images, the endpoints of the line segment may be truncated in the 2D projections by chance. Such discrepancies can severely impact the

*Corresponding author.

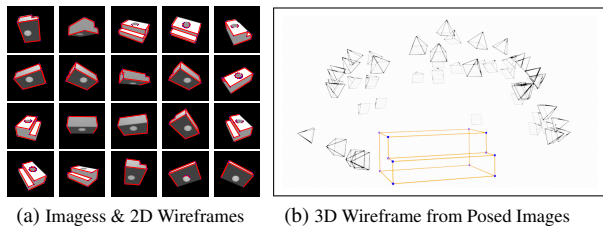


Figure 2. **Illustrative Overview** of the problem of 3D wireframe reconstruction. Given a set of posed images and the corresponding 2D wireframe detection results in (a), the proposed NEAT estimates the 3D wireframe representation of the scene in (b).

accuracy of the reconstruction, as the matching process relies on these endpoints to accurately represent the 3D geometry. These matching-based methods often result in incomplete 3D line models or suffer from fragmentation and noise, depending on the choice of 2D detectors [25, 36, 43–46] and matchers [23, 24] of line segments, as in Fig. 1.

Dense Fields of Sparse Geometries. We challenge the explicit matching pipeline of 3D wireframe reconstruction from the perspective of dense field representation. We draw inspiration from the “**implicit matching**” capacity [42] of the emerging neural implicit fields [2, 22, 49] for 3D dense representations (e.g., density fields and signed distance functions), and propose to *render* 3D line segments from multi-view 2D observations. Such a basic idea roughly works by leveraging a coordinate MLP to render 3D line segments from 2D observations, but remains problematic due to the entailed view-by-view rendering of 3D line segments in two-fold: (1) the 2D line segments of a detected wireframe often undergo localization errors, resulting in erroneous 3D line segment predictions via view-by-view rendering, and (2) simply stacking the rendered 3D line segments from all views leads to a very large amount of 3D line segments, requiring non-trivial merging/fusion to form a 3D wireframe representation of the scene.

Line-to-Point Attraction in Neural Fields. We tackle the above issues by leveraging the line-to-point attraction that inherently persists in the wireframe representation, in which *every endpoint of a 3D line segment should be in the set of 3D junctions of the underlying scene*. Based on this, we formulate the two types of entities of 3D wireframes, the 3D line segments and junctions, in a novel *rendering-distilling* formulation, where the sparse set of 3D line segments are represented in a dense neural field while the junctions play the role of distilling a sparse wireframe structure from the fields. Our work is entitled as *NEural Attraction* (NEAT) for 3D wireframe reconstruction, mainly because of the neural design of the 3D line segments and junctions, and of leveraging the line-to-point attraction to enable joint optimization of the neural networks from multi-view images and its 2D wireframe detection results. To the best

of our knowledge, we accomplish the first matching-free solution of 3D wireframe/line reconstruction by learning and optimizing from random initializations without any 3D scene information required.

In experiments, we showcase that our matching-free NEAT solution significantly outperforms all the matching-based approaches with accurate yet complete 3D wireframe reconstruction results on both the DTU [1] and BlendedMVS [47] datasets, working well in both straight-line dominated scenes and curve-based (or polygonal line segment dominated) scenes that challenges the traditional matching-based approaches, paving a way towards learning 3D primal sketch in a more general way. Furthermore, we show that the neurally perceived 3D junctions is applicable to the recently proposed 3D Gaussian Splatting [13] as better initialization than the COLMAP [29] with about 20 times fewer points, showing case the potential of structured and compact 3D reconstruction.

2. Related Work

Structured 3D Reconstruction in Geometric Primitives.

Because of the inherent structural regularities for scene representation conveyed by line structures [10, 16, 19, 28, 31] and planar structures [33, 34], there has been a vast body of literature on line-based multiview 3D reconstruction tasks including single-view 3D reconstruction [18, 33], line-based SfM [3, 27], SLAM [26, 38], and multi-view stereo [12, 17, 39] based on the theory of multi-view geometry [11]. Due to the challenge of line segment detection and matching in 2D images, most of those studies expected the 2D line segments detected from input images to be redundant and small-length to maximize the possibility of line segment matching. As for the estimation of scene geometry and camera poses, the keypoint correspondences (even including the 3D point clouds) are usually required. For example in Line3D++ [12], given the known camera poses by keypoint-based SfM systems [29, 30, 32, 40], it is still challenging though to establish reliable correspondences for the pursuit of structural regularity for 3D line reconstruction. For our goal of 3D wireframe reconstruction, because 2D wireframe parsers aim at producing parsimonious representations with a small number of 2D junctions and long-length line segments, those correspondence-based solutions pose a challenging scenario for cross-view wireframe matching, thus leading to inferior results than the ones using redundant and small-length 2D line segments detected by the LSD [36]. To this end, we present a correspondence-free formulation based on coordinate MLPs, which provides a novel perspective to accomplish the goal of 3D wireframe reconstruction from the parsed 2D wireframes.

Neural Rendering for Geometric Primitives. In recent years, the emergence of neural implicit representations [2,

[20, 21, 48] have greatly renoun the 3D vision community. By using coordinate MLPs to implicitly learn the scene geometry from multi-view inputs without knowing either the cross-view correspondences or the 3D priors, it has largely facilitated many 3D vision tasks including novel view synthesis, multi-view stereo, surface reconstruction, *etc.* Some recent studies further exploited the neural implicit representations by (explicitly and implicitly) taking the geometric primitives such as 2D segmentation masks into account to lift the 2D detection results into 3D space for scene understanding and interpretation [8, 15, 37, 41]. Most recently, nerf2nerf [9] exploited a geometric 3D representation, surface fields as a drop-in replacement for point clouds and polygonal meshes, and takes the keypoint correspondences to register two NeRF MLPs. Our study can be categorized as the exploration of geometric primitives in neural implicit representation, but we focus on computing a parsimonious representation by using the most fundamental geometric primitives, the junction (points) and line segments, to provide a compact and explicit representation from coordinate MLPs.

3. NEAT of 3D Wireframe Reconstruction

In this section, we formulate the problem of 3D wireframe reconstruction, lying on the high-level idea of approaching the goal of using volume rendering instead of the explicit line segment matching to build a unified 3D computational representation of line segments and junctions from the 2D detected wireframes.

Problem Statement. For the problem illustrated in Fig. 2, we present our approach for 3D wireframe reconstruction from n -view posed images, $\{\mathcal{I}_i\}_{i=1}^n$. Each image \mathcal{I}_i is characterized by intrinsic and extrinsic matrices. We use the HAWPv3 model [46] to detect 2D wireframes in these images, represented as undirected graphs $G_i = (V_i, E_i)$. The goal is to construct a 3D wireframe graph $\mathcal{G} = (\mathcal{V}, \mathcal{E})$, translating these 2D wireframes into a 3D representation with \mathcal{V} as 3D junctions and \mathcal{E} as the 3D line segments.

Method Overview. Our NEAT method is built on the VolSDF framework [49] with two primary neural components: (1) a Neural Attraction Field for 3D line segments, and (2) a Global 3D Junction Perceiver (GJP). These components work jointly to create NEAT 3D wireframe models from the 2D wireframe observations. We start by learning a dense representation of 3D line segments from 2D wireframes using the Neural Attraction Field, as visualized in Figure 3. This is followed by the Global 3D Junction Perceiver, which identifies a set of 3D junctions. As a final step of the wireframe reconstruction, the perceived 3D junctions play in a distillation role to clean up the optimized NEAT field. In implementation, we adopt a simple design for the MLPs used in the SDF and radiance field, aligned with VolSDF specifications. For the

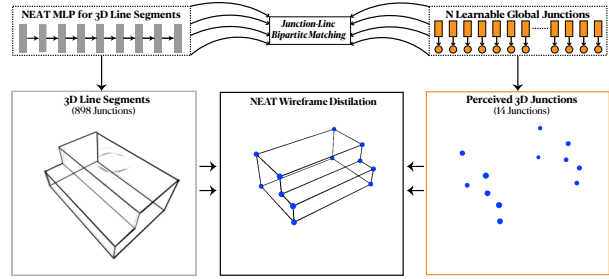


Figure 3. The proposed NEAT field learning framework for 3D wireframe reconstruction. In the top, the neural design of NEAT MLP and the predefined N global junctions are illustrated, these two components are “attracted” by the junction-to-line bipartite matching, resulting a rendering-yet-distillation formulation to render 3D line segments in NEAT MLP as a dense representation of 3D line segments, and then distilled by the learned 3D global junctions for wireframe reconstruction.

NEAT field, a 4-layer MLP renders the 3D line segments. Additional implementation details and hyperparameters are outlined in the Appendix B.3.

3.1. Rendering 3D Line Segments from 2D

We propose to leverage the power of “implicit matching” ability of neural fields to obtain 3D line segments. Our method is built on the basic formulation of VolSDF [49] that renders a ray $\mathbf{x}_t = \mathbf{c} + t \cdot \mathbf{v}$ emanating from the camera location $\mathbf{c} \in \mathbb{R}^3$ with the (unit) view direction $\mathbf{v} \in \mathbb{R}^3$ to estimate the image appearance by,

$$\hat{I}(\mathbf{c}, \mathbf{v}) = \int_0^\infty T(t) \cdot \sigma(x_t) \cdot \mathbf{r}(x_t, \mathbf{v}, \mathbf{n}(x_t), z(x_t)) dt, \quad (1)$$

where $\mathbf{r}(\cdot)$ is the radiance of the ray x_t , and $T(t)$ is the transmittance $T(t) = \exp - \int_0^t \sigma(x(s)) ds$ along the ray from camera center to t , the density field $\sigma(\cdot)$ is transformed by the signed distance function $d_\Omega(\mathbf{x})$ of an implicit field using,

$$\sigma(\mathbf{x}) = \frac{1}{\beta} \Psi_\beta(-d_\Omega(\mathbf{x})), \quad (2)$$

with the learnable scaling factor β . As for the optimization of SDF and radiance fields, the image loss \mathcal{L}_{img} between the rendered image \hat{I} and its corresponding ground-truth \mathcal{I} , and Eikonal loss \mathcal{L}_{eik} for SDF network are used.

Neural Attraction Fields. In our NEAT method, we adapt volume rendering, typically used for optimizing dense 3D representations like density fields and SDFs, to focus on 3D line segments and junctions. Our approach is inspired by the dense attraction field representations used in 2D line segment detection and wireframe parsing, as extensively researched in previous studies [44, 46]. As illustrated in

Fig. 3 using a synthetic example, we utilize the attracted pixels of 2D line segments in each image to define the rays for 3D rendering. For each segment, its attracted pixels are projected perpendicularly onto the 2D segment. This projection is confined within the endpoints of the segment with respect to a predefined distance threshold, τ_{ray} . Each pixel is associated with its nearest line segment, ensuring a dense coverage of supporting areas for the segments. This approach facilitates the volume rendering of 3D line segments by providing a robust underlying structure.

In our approach, we model a 3D line segment at any point \mathbf{x}_t along a ray. The endpoint displacements $(\Delta\mathbf{x}_t^1, \Delta\mathbf{x}_t^2)$ relative to \mathbf{x}_t are computed as,

$$(\Delta\mathbf{x}_t^1, \Delta\mathbf{x}_t^2) = L(\mathbf{x}_t) \in \mathbb{R}^{2 \times 3}, \quad (3)$$

yielding the two endpoints of the segment by $(\mathbf{x}_t + \Delta\mathbf{x}_t^1, \mathbf{x}_t + \Delta\mathbf{x}_t^2)$. The mapping function $L(\cdot)$ is parameterized by a 4-layer coordinate MLP. It incorporates the view direction \mathbf{v} , the surface normal $\mathbf{n}(\cdot)$ from the SDF gradient, and a 128-dimensional feature vector $\mathbf{z}(\mathbf{x}_t)$ from the SDF network, reflecting the view-dependent nature of 2D line segments. For rendering a 3D line segment, we apply the equation,

$$(\mathbf{x}^s, \mathbf{x}^t) = \int_0^\infty T(t)\sigma(t)(L(\mathbf{x}_t) + \mathbf{x}_t) dt. \quad (4)$$

Here, \mathbf{x}^s and \mathbf{x}^t are the 3D endpoints for the attraction pixel \mathbf{x} of a 2D line segment $\tilde{l} = (j_1, j_2) \in V_i \times V_i$ of the i -th view, calculated along its ray \mathbf{x}_t .

According to the pixel-to-line relationship defined by 2D attraction field representations, the rendered 3D line segment $(\mathbf{x}^s, \mathbf{x}^t)$ of a ray \mathbf{x}_t should be consistent with $\tilde{l} = (j_1, j_2)$, thus resulting in a loss function between the projected 2D endpoints by viewpoint projection $\Pi(\cdot)$ and \tilde{l} in,

$$\mathcal{L}_{\text{neat}} = \|\Pi(\mathbf{x}^s) - j_1\|^2 + \|\Pi(\mathbf{x}^t) - j_2\|^2. \quad (5)$$

The proposed Neural Attraction Fields of 3D line segments is optimized together with SDF and the radiance field by minimizing the loss functions stated above, forming a queryable and dense representation of 3D line segments.

Minimizing the loss functions $\mathcal{L}_{\text{neat}}$, \mathcal{L}_{img} , and \mathcal{L}_{eik} allows us to derive a geometrically meaningful but noisy 3D line cloud from multi-view images, as demonstrated in Fig. 4 using both a synthetic example and a real case from the DTU-24 scene [1]. The absence of explicit line matching across multiple views leads to duplication of the same 3D line segments, each with its own view-dependent prediction errors. In the following section, we discuss how this redundancy and noise, while initially seeming detrimental, actually provide a strong inductive bias towards achieving the goal of 3D wireframe reconstruction.

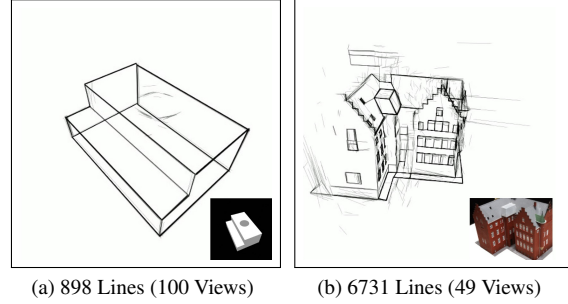


Figure 4. Two cases of learned noisy and redundant 3D line segments by line segment rendering. The case (a) takes the images and line segments introduced in Fig. 2a, and the case (b) is a real-world case of DTU-24 scene.

3.2. Neural 3D Junction Perceiver

This section introduces our method to “clean up” the noisy and redundant 3D line cloud created by Neural Attraction Fields. Leveraging the relationship between 3D junctions and line segments in wireframes, we propose a neural and joint optimization approach, central to our NEAT method. Using the 3D line cloud, denoted by \mathbf{L}_{neat} , a query-based learning method is designed for perceiving 3D junctions (Eq. (6)) via junction-line attraction, which plays the role of distillation for 3D wireframe reconstruction.

Global 3D Junction Perceiving. Our 3D line segment rendering inherits the dense representation as the density field and the radiance field. To achieve parsimonious wireframes, we propose a novel query-based design to holistically perceive a predefined sparse set of N 3D junctions by

$$Q_{N \times C} \xrightarrow{\text{MLP}} J_{N \times 3}, \quad (6)$$

where $Q_{N \times C}$ are C -dim latent queries (randomly initialized in learning). Surprisingly, as we shall show in experiments, the underlying 3D scene geometry induced synergies between $J_{N \times 3}$ and the above 3D line segment rendering integral enable us to learn a very meaningful global 3D junction perceiver.

In the absence of well-defined ground-truth for learning 3D junctions, we use the endpoints of redundant rendered 3D line segments (Sec. 3.1) as noisy labels. By reshaping the line cloud \mathbf{L}_{neat} into $\mathbf{J}_{\text{neat}} \in \mathbb{R}^{2M \times 3}$, our process involves two steps: (1) clustering $\mathbf{J}_{2M \times 3}$ using DBScan to yield pseudo 3D junctions $\mathbf{J}_{\text{cls}} \in \mathbb{R}^{m \times 3}$ with $m < 2M$ clusters; (2) applying bipartite set-to-set matching between the perceived junctions $J_{N \times 3}$ (Eq. (6)) and \mathbf{J}_{cls} using the Hungarian algorithm. The matching cost is based on the ℓ_2 norm between 3D points. We define $\mathcal{J} = \{(J_k, \mathbf{J}_{i_k}^{\text{cls}}) | k = 1, \dots, K\}$ as the set of matched junctions, where $K = \min(N, m)$, and i_k is the index of the k -th matched pseudo label $\mathbf{J}_{i_k}^{\text{cls}}$. Then, our goal is to minimize the distance

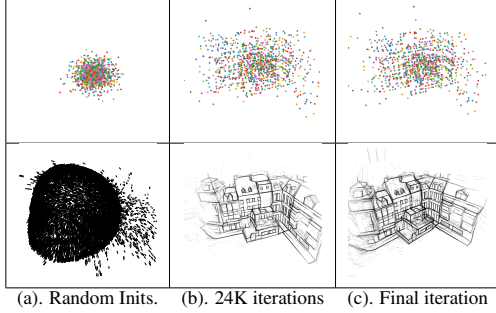


Figure 5. **Optimization Process** of 3D Junction Perceiving (top) from the noisy 3D line cloud (bottom) on the DTU-23 scene.

between matched junctions and their corresponding pseudo labels using

$$\mathcal{L}_{jc}(J_k, \mathbf{J}_k) = \|J_k - \mathbf{J}_k\|_1 + \lambda \cdot \|\Pi(J_k) - \Pi(\mathbf{J}_k)\|_1, \quad (7)$$

where $\Pi(\cdot)$ is the 3D-to-2D projection, and λ the trade-off parameters (e.g. 0.01 in our experiments).

Joint Optimization. In our final implementation, we refine our approach by jointly optimizing the NEAT field and the 3D junction perceiver. This optimization involves minimizing all aforementioned loss functions in a weighted sum, which allows for dynamic distillation of 3D junctions from the noisy 3D line cloud generated by the NEAT field. The total loss function, \mathcal{L}_{total} , is expressed as:

$$\mathcal{L}_{total} = \mathcal{L}_{img} + \lambda_e \mathcal{L}_{eik} + \lambda_n \mathcal{L}_{neat} + \lambda_j \mathcal{L}_{jc}, \quad (8)$$

where \mathcal{L}_{img} and \mathcal{L}_{eik} are as defined in [49]. The weights λ_n, λ_e , and λ_j are all set to 0.01. As depicted in Figure 5, this optimization process continually refines the global 3D junctions by extracting them from the 3D line cloud of NEAT field at each iteration, all trained from scratch.

3.3. NEAT Wireframe Distillation using Junctions

After training, we acquire N 3D junctions $J_{N \times 3}$ and M 3D line segments $\mathbf{L}_{neat} \in \mathbb{R}^{M \times 2 \times 3}$. The line segments are indexed by 3D junctions based on their spatial relationship, assigning each segment \mathbf{L}_{neat}^i a global ID within $(u, v) \in \{0, \dots, N-1\} \times \{0, \dots, N-1\}$, with $u < v$. Indexing is informed by endpoint distances. Segments with angular distances over 10 degrees or perpendicular distances above 0.01 units in 3D space are deemed "too far" and removed, ensuring alignment with the 3D junctions. Further details are available in Appendix B.

Endpoint indexing significantly reduces the number of 3D line segments. Segments like $(\mathbf{x}_i^s, \mathbf{x}_i^t)$ and $(\mathbf{x}_j^s, \mathbf{x}_j^t)$ sharing the same junction IDs $(u_i, v_i) = (u_j, v_j) = (u, v)$ are grouped under one global line segment defined by (u, v) . We represent these grouped segments as $\mathbf{L}_{u,v} = \{\mathbf{l}_{u,v}^1, \dots, \mathbf{l}_{u,v}^T\} \in \mathbb{R}^{T \times 2 \times 3}$, where $T = T_{u,v}$ indicates the

count of segments in $\mathbf{L}_{u,v}$. For convenience, the global line segment for index (u, v) is denoted as $\mathbf{l}_{u,v}^0 = (J_u, J_v)$. Junctions not indexed by more than one line segment in \mathbf{L}_{neat} are marked as inactive.

The 3D Wireframe. After indexing the 3D line segments \mathbf{L}_{neat} with global junctions, we form the graph $\mathcal{G} = (\mathcal{V}, \mathcal{E})$ composed of active global junctions and their index pairs. To refine this graph, we remove isolated junctions and line segments, resulting in the final 3D wireframe \mathcal{G} , where $\mathcal{V} \subset \mathbb{R}^3$ represents the vertices and $\mathcal{E} \subset \mathbb{Z}^2$ the edges.

Least Square Optimization of 3D Junctions. Given that 3D junctions are derived from a noisy 3D line cloud, we optimize them by leveraging their relationships with global line segments (J_u, J_v) and corresponding 3D line segments $\mathbf{L}(u, v)$. This alignment aims to match junctions with their supporting 3D line segments. The optimization is framed as a non-linear least squares problem with the cost function $\mathcal{L}(J)$, defined as:

$$\mathcal{L}(J) = \sum_{(u,v)} \sum_{i=1}^{T_{u,v}} d_{ang}(\mathbf{l}_{u,v}^0, \mathbf{l}_{u,v}^i)^2 + d_{perp}(\mathbf{l}_{u,v}^0, \mathbf{l}_{u,v}^i)^2, \quad (9)$$

where d_{ang} and d_{perp} represent the angular and perpendicular distances between two 3D line segments, respectively. The optimization details are provided in Appendix C.

The Final Wireframe. After leveraging the least square optimization to adjust the position 3D junctions, we further remove the isolated junctions and the isolated line segments in \mathcal{G} of which their projection to 2D space are not supported by any line segment of the 2D wireframe observations. Here, the criterion of the support is defined by the minimum angular distance and the perpendicular distance between the projected 3D line segment and the 2D line segment is not more than 10 degree and 5 pixels, respectively. After the filtering, we adjust the activated 3D junctions by querying SDF, see Appendix C for details.

4. Experiments

In experiments, we mainly testify our NEAT on two datasets (*i.e.*, the DTU dataset [1] and the BMVS dataset [47]) for real-scene multiview images with known camera poses. In addition to those two datasets, in Appendix D, the experiments on the ABC dataset [14] evaluated by using the 3D wireframe annotations further verified our proposed NEAT approach for the 3D wireframe representation.

4.1. Baselines, Datasets and Evaluation Metrics

We take the well-engineered Line3D++ [12] and the recently-proposed LiMAP [17] as the baselines to make quantitative and qualitative comparisons, all of which are mainly designed for line-based 3D reconstruction based on two-view line matching results. Because our target is

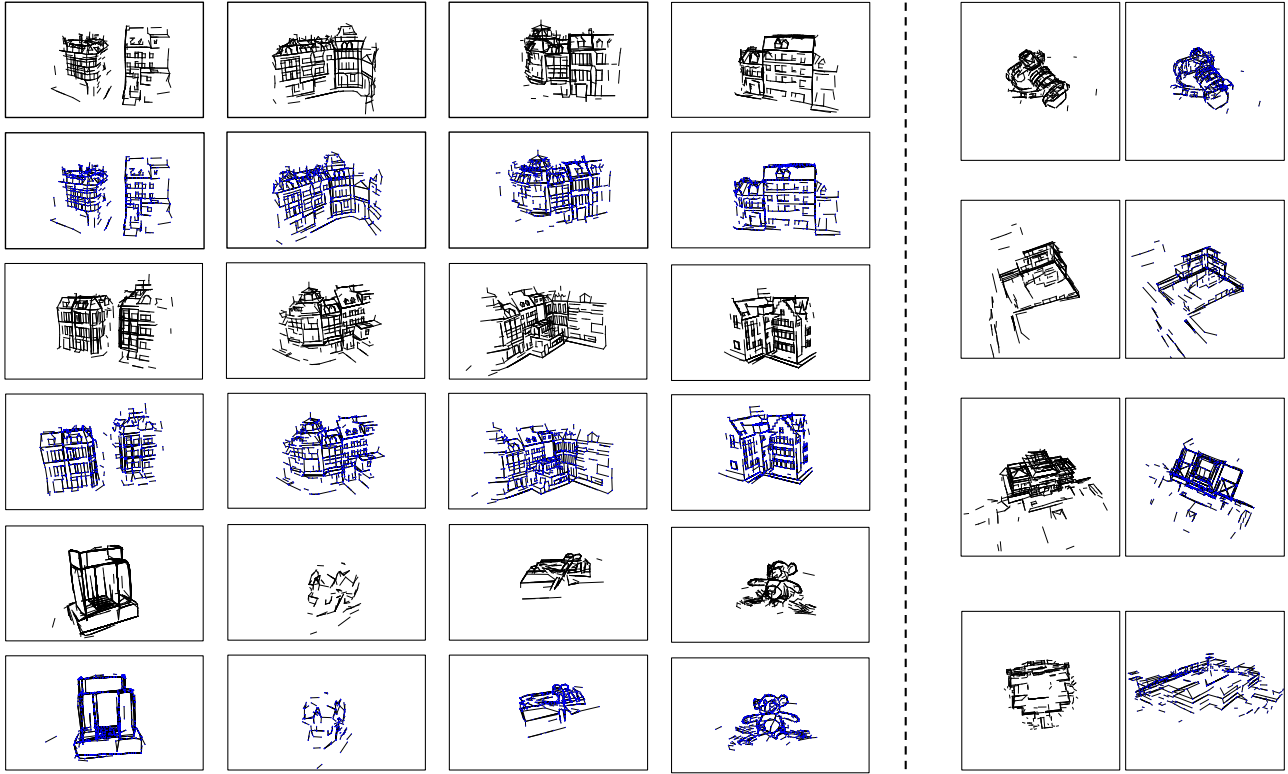


Figure 6. **Visualization of 3D Wireframe Reconstruction** on the 12 scenes from the DTU dataset [1] and the 4 scenes from the BlendedMVS dataset [47]. For each scene, we show its line segment view (by hiding the junctions) in black, and the wireframe view by coloring the junctions in blue. For the comparison, please see our [video](#).

Table 1. Evaluation Results on the DTU and BlendedMVS datasets for the reconstructed 3D wireframes. ACC-J and ACC-L are the evaluation for junctions and line segments. For Line3D++@HAWP, LiMAP and ELSR, all the endpoints of line segments are treated as junctions.

Scan	NEAT (Ours)					LiMAP [17]				Line3D++@HAWP			
	ACC-J ↓	ACC-L	COMP-L ↓	#Lines ↑	#Junctions	ACC-J ↓	ACC-L	COMP-L ↓	#Lines ↑	ACC-J ↓	ACC-L ↓	COMP-L ↓	#Lines ↑
DTU Dataset [1]													
Avg.	0.7718	0.8002	6.1064	624	503	1.0944	0.8547	7.7756	231	0.9019	0.8133	8.5086	249
16	0.8263	0.7879	5.4135	729	554	1.0385	0.7898	6.0420	335	0.7957	0.6992	6.9052	388
17	0.7754	0.6695	5.0498	738	546	1.1015	0.8804	5.8212	388	0.8816	0.7778	7.6257	395
18	0.6429	0.6868	5.3796	701	596	0.9950	0.8253	7.0154	287	0.7894	0.7528	7.7082	305
19	0.6989	0.6923	4.6529	809	510	0.7689	0.7110	7.9461	160	0.6815	0.7953	6.9776	330
21	0.9042	0.6923	4.6529	809	571	1.1011	0.8884	5.9821	319	0.9064	0.7953	6.9776	330
22	0.6343	0.6910	5.0871	758	596	0.8998	0.7353	6.8567	281	0.7494	0.7079	7.8014	328
23	0.5882	0.6193	5.5992	771	597	1.0561	0.8293	6.5078	377	0.8005	0.7356	8.2679	320
24	0.6386	0.5944	5.9104	860	549	1.0314	0.8293	6.5078	377	0.7940	0.6807	7.6886	366
37	1.4815	1.0856	7.5362	420	405	1.2721	1.2352	8.6413	120	1.1796	1.0287	10.2244	60
40	0.6298	1.0354	8.7825	137	469	1.2108	0.8327	9.9988	41	0.8486	0.6877	10.1206	83
65	0.7212	1.0354	8.7825	137	171	1.0469	0.5071	11.1936	7	1.1008	1.0697	11.1519	23
105	0.7204	1.0127	6.4296	621	478	1.6108	1.1929	10.7943	90	1.2957	1.0286	10.6539	61
BlendedMVS Dataset [47]													
Avg.	0.1949	0.1802	6.4621	602	514	0.3712	0.3169	6.9415	313	0.3743	0.3545	6.8760	724
1	0.0365	0.0404	3.7253	653	565	0.0488	0.0651	5.0457	226	0.0682	0.0650	5.3625	691
2	0.1715	0.1585	8.2943	328	343	0.3478	0.2817	8.7663	195	0.4327	0.4174	8.8864	396
3	0.2564	0.2165	7.5600	931	664	0.3796	0.3162	7.5366	467	0.3795	0.3582	7.3192	931
4	0.3153	0.3055	6.2686	509	483	0.7086	0.6045	6.4174	365	0.6171	0.5774	5.9359	876

3D wireframe reconstruction instead of 3D line segment reconstruction, for fair comparisons, we use HAWPv3 [46] as the alternative for 2D detection in the use of Line3D++

and LiMAP. For those baselines, we use their official implementation for 3D line segments reconstruction.

DTU [1] and BlendedMVS [47] Datasets. These two

datasets were mainly designed for multiview stereo (MVS), but they are applicable to 3D wireframe reconstruction as they provided high-quality 3D point clouds as annotations. For our experiments, we run our method on 12 scenes from DTU datasets and 4 scenes from BlendedMVS datasets. For the quantitative evaluation, we first convert the reconstructed wireframe model by NEAT (or the 3D line segment model by baselines) into the point cloud by sampling 32 points on each line segment and computing the ACC metric to make comparisons. Because the reconstructed 3D wireframes (and line segments) are rather sparse than the dense surfaces, the COMP metric used for comparison would be less informative than ACC. Therefore, we additionally use the number of reconstructed 3D line segments and junctions as the reference of completeness.

4.2. Main Comparisons

We compare our NEAT approach with three baselines on the scenes from DTU and BlendedMVS datasets, which include both the straight-line dominant scenes and some curve-based ones. In Tab. 1, we quantitatively report the ACCs for both 3D line segments and their junctions (or endpoints), as well as the number of geometric primitives. Compared to the baseline *Line3D++@HAWP* that takes the same 2D wireframes as input, our NEAT significantly outperforms it in all metrics, which indicates that NEAT is able to yield more accurate and complete 3D reconstruction results than L3D++ for HAWP inputs. Fig. 6 visualizes the reconstructed 3D wireframes for the evaluated scenes on the DTU and BlendedMVS datasets.

4.3. Ablation Studies

In our ablation study, two scenes (*i.e.*, DTU-24 and DTU-105) are used as representative cases to discuss our NEAT approach. In the first, we qualitatively show the NEAT lines (*i.e.*, raw output of 3D line segments by querying the NEAT field), the initial reconstruction by binding the queried NEAT lines to global junctions, and the final reconstruction results by the visibility checking. Then, we discuss our NEAT approach in the following two aspects: (1) the parameterization of NEAT Fields and (2) the view dependency issue for junction perceiving. For more ablation studies for the hyperparameter setting, especially for the number of global junctions, please refer to Appendix C.

The Process of Wireframe Reconstruction. Fig. 7 shows the three components for wireframe reconstruction. In the first component, we query all possible 3D line segments from the optimized NEAT field. In the second component, the queried 3D line segments are binding to the global junctions. In the third step, by leveraging the non-linear optimization and a relaxed visibility checking, the unstable 3D line segments are removed from the initial wireframe models. Benefitting from the proposed novel mechanism of

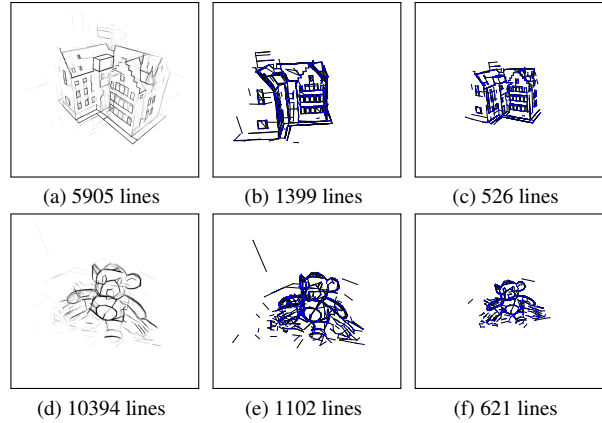


Figure 7. Left: NEAT lines (by coordinate MLP); Middle: initial wireframes (without visibility checking); Right: the final wireframes (with visibility checking) in the right.

Table 2. Quantitatively evaluation results for ablation studies on the DTU-24 and DTU-105 scenes.

	View Dir.	Clustering	ACC (J)↓	ACC (L)↓	# Lines	# Junctions
DTU-24	No	No	0.925	0.847	744	531
	Yes	No	0.796	0.678	827	475
	Yes	Yes	0.639	0.594	860	549
DTU-105	No	No	0.822	1.209	607	499
	Yes	No	0.749	1.154	557	408
	Yes	Yes	0.720	1.013	621	478

learning global 3D junctions, we largely simplified the way of removing duplicated and unreliable line segments without using either the known 3D points or the complicated line segment matching.

Parameterization of NEAT Fields. We found that the parameterization of NEAT Fields learning is playing in a vital role in the wireframe reconstruction. Even though our NEAT field aims at representing 3D line segments by the displacement vectors of the 3D points, the localization error in the detected 2D wireframes will possibly lead to some 3D line segments that cannot be well supported by high-quality 2D detection results missing. The information on view direction is a key factor to avoid this issue and yield more complete results. According to Tab. 2, the parameterization without the viewing directions will result in a coarser reconstruction with larger ACC errors for both 3D junctions and line segments while having fewer line segments although the number of global junctions is similar to the final model.

Clustering in Junction Perceiving. The DBScan [7] clustering is a key factor in accurately perceiving global junctions from the view-dependent coordinate MLP of the NEAT field. To verify this factor, we ablated the DBScan clustering to optimize MLPs on DTU-24 and DTU-105. Quantitatively reported in Tab. 2, although the parameterization of viewing direction largely reduced the ACC errors for both reconstructed junctions and line

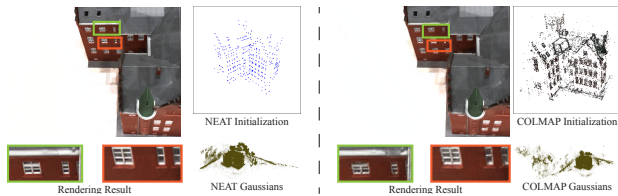


Figure 8. NEAT is applicable to 3D Gaussian Splatting framework to obtain more meaningful 3D Gaussian ellipsoids for better rendering results using 20 times fewer initial 3D points.

segments, the number of 3D junctions and line segments is also significantly reduced. When we enable the clustering during optimization, the lower-quality 3D local junctions (from the NEAT field) can be filtered, thus leading to an easy-to-optimize mode to yield more 3D junctions and line segments with fewer reconstruction errors.

4.4. NEAT for 3D Gaussian Splatting

Recently, 3D Gaussian Splatting [13] has become popular in neural rendering, owing to its computational efficiency and high-quality rendering. Our proposed NEAT method effectively represents 3D scenes using a limited number of junctions and line segments in wireframe format. We explored whether these reconstructed 3D junctions and line segments enhance novel view synthesis in 3D Gaussian Splatting [13] and found positive results. As demonstrated in Fig. 8, the final 3D Gaussian ellipsoids, optimized using different initialization (i.e., SfM Points and NEAT junctions), show that using only 549 points from the 3D junctions can yield more accurate geometry of Gaussian ellipsoids, thus improving rendering quality. Due to space constraints, further rendering experiments using NEAT’s output are detailed in the Appendix E.

4.5. Failure Mode and Limitations

Volume Rendering of NEAT Fields. Our method, based on VolSDF [49], faces inherent difficulties in inside-out scenes for neural surface rendering, similar to recent studies [50]. Overcoming these challenges, though possible with techniques like pre-trained monocular depth and normal maps [6], is beyond this paper’s scope and reserved for future work.

2D Detection Results are Critical. Another critical issue is the quality of 2D wireframe detection. Failures in the HAWP model [46] directly impact our 3D wireframe reconstruction and parsing goals. Fig.9 illustrates a failure case from the ScanNet[5] dataset, highlighting issues like motion blur affecting wireframe detection and leading to inaccuracies in 3D line segments. Despite these challenges, our global junctions (Fig. 9d) show potential in learning from blurry 2D wireframes, suggesting new insights into the relationship between junctions and line segments in wireframe representation.

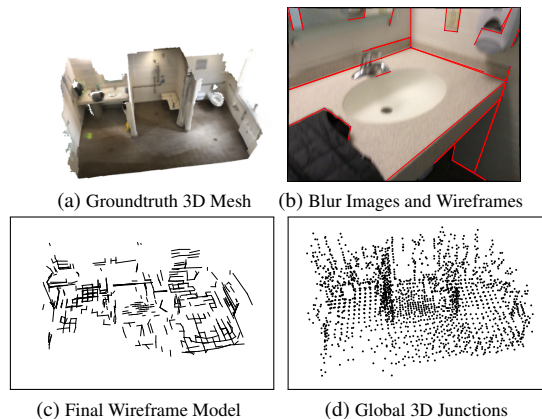


Figure 9. A Representative Failure Mode on ScanNet.

The Scalability Issue. Our proposed method is currently limited by the predefined number of 3D global junctions (e.g. 1024 junctions), which would be challenged in large-scale scenes that apparently contain much more 3D junctions. Though this limitation can be alleviated by leveraging a divide-and-conquer strategy like Block-NeRF [35], the number of junctions should be scene-dependent and be automatically determined instead of being treated as a predefined hyperparameter in the future work.

5. Conclusion

This paper studied the problem of multi-view 3D wireframe parsing (reconstruction) to provide a novel viewpoint for compact 3D scene representation. Building on the basis of the volumetric rendering formulation, we propose a novel NEAT solution that simultaneously learns the coordinate MLPs for the implicit representation of the 3D line segments, and the global junction perceiving (GJP) to explicitly learn global junctions from the randomly-initialized latent arrays in a self-supervised paradigm. Based on new findings, we finally achieve our goal of computing a parsimonious 3D wireframe representation from 2D images and wireframes without considering any heuristic correspondence search for 2D wireframes. To our knowledge, we are the first to achieve multi-view 3D wireframe reconstruction with volumetric rendering. Our proposed novel junction perceiving module opens a door to characterize the scene geometry from 2D supervision in structured point-level 3D representation.

Acknowledgment. N. Xue was partially supported by the NSFC under Grant 62101390. T. Wu was supported in part by NSF IIS-1909644. We would like to thank anonymous reviewers for their constructive suggestions. The views presented in this paper are those of the authors and should not be interpreted as representing any funding agencies.

References

- [1] Henrik Aanaes, Rasmus Ramsbøl Jensen, George Vogiatzis, Engin Tola, and Anders Bjorholm Dahl. Large-scale data for multiple-view stereopsis. *Int. J. Comput. Vis.*, 120(2):153–168, 2016. [2](#), [4](#), [5](#), [6](#), [1](#)
- [2] Jonathan T. Barron, Ben Mildenhall, Matthew Tancik, Peter Hedman, Ricardo Martin-Brualla, and Pratul P. Srinivasan. Mip-nerf: A multiscale representation for anti-aliasing neural radiance fields. In *IEEE/CVF International Conference on Computer Vision (ICCV)*, pages 5835–5844, 2021. [2](#)
- [3] Manmohan Krishna Chandraker, Jongwoo Lim, and David J. Kriegman. Moving in stereo: Efficient structure and motion using lines. In *IEEE/CVF International Conference on Computer Vision (ICCV)*, pages 1741–1748, 2009. [2](#)
- [4] Blender Online Community. *Blender - a 3D modelling and rendering package*. Blender Foundation, Stichting Blender Foundation, Amsterdam, 2018. [4](#)
- [5] Angela Dai, Angel X. Chang, Manolis Savva, Maciej Halber, Thomas A. Funkhouser, and Matthias Nießner. Scannet: Richly-annotated 3d reconstructions of indoor scenes. In *IEEE/CVF Conference on Computer Vision and Pattern Recognition (CVPR)*, pages 2432–2443, 2017. [8](#)
- [6] Ainaz Eftekhari, Alexander Sax, Jitendra Malik, and Amir Zamir. Omnidata: A scalable pipeline for making multi-task mid-level vision datasets from 3d scans. In *IEEE/CVF International Conference on Computer Vision (ICCV)*, pages 10766–10776, 2021. [8](#)
- [7] Martin Ester, Hans-Peter Kriegel, Jörg Sander, and Xiaowei Xu. Density-based spatial clustering of applications with noise. In *International Conference on Knowledge Discovery and Data Mining (KDD)*, 1996. [7](#), [2](#)
- [8] Xiao Fu, Shangzhan Zhang, Tianrun Chen, Yichong Lu, Lanyun Zhu, Xiaowei Zhou, Andreas Geiger, and Yiyi Liao. Panoptic nerf: 3d-to-2d label transfer for panoptic urban scene segmentation. In *International Conference on 3D Vision (3DV)*, pages 1–11, 2022. [3](#)
- [9] Lily Goli, Daniel Rebain, Sara Sabour, Animesh Garg, and Andrea Tagliasacchi. nerf2nerf: Pairwise registration of neural radiance fields. In *IEEE International Conference on Robotics and Automation (ICRA)*, 2023. [3](#)
- [10] Adolfo Guzmán. Decomposition of a visual scene into three-dimensional bodies. In *Fall Joint Computer Conference*, pages 291–304, 1968. [2](#)
- [11] Richard Hartley and Andrew Zisserman. *Multiple View Geometry in Computer Vision*. Cambridge university press, 2003. [2](#)
- [12] Manuel Hofer, Michael Maurer, and Horst Bischof. Efficient 3d scene abstraction using line segments. *Comput. Vis. Image Underst.*, 157:167–178, 2017. [1](#), [2](#), [5](#), [4](#)
- [13] Bernhard Kerbl, Georgios Kopanas, Thomas Leimkühler, and George Drettakis. 3d gaussian splatting for real-time radiance field rendering. *ACM Transactions on Graphics*, 42(4), 2023. [2](#), [8](#), [5](#)
- [14] Sebastian Koch, Albert Matveev, Zhongshi Jiang, Francis Williams, Alexey Artemov, Evgeny Burnaev, Marc Alexa, Denis Zorin, and Daniele Panozzo. ABC: A big CAD model dataset for geometric deep learning. In *IEEE/CVF Conference on Computer Vision and Pattern Recognition (CVPR)*, pages 9601–9611, 2019. [5](#), [1](#)
- [15] Abhijit Kundu, Kyle Genova, Xiaoqi Yin, Alireza Fathi, Caroline Pantofaru, Leonidas J. Guibas, Andrea Tagliasacchi, Frank Dellaert, and Thomas A. Funkhouser. Panoptic neural fields: A semantic object-aware neural scene representation. In *IEEE/CVF Conference on Computer Vision and Pattern Recognition (CVPR)*, pages 12861–12871, 2022. [3](#)
- [16] David C. Lee, Martial Hebert, and Takeo Kanade. Geometric reasoning for single image structure recovery. In *IEEE/CVF Conference on Computer Vision and Pattern Recognition (CVPR)*, pages 2136–2143, 2009. [2](#)
- [17] Shaohui Liu, Yifan Yu, Rémi Pautrat, Marc Pollefeys, and Viktor Larsson. 3d line mapping revisited. In *IEEE Conf. Comput. Vis. Pattern Recog.*, pages 21445–21455. IEEE, 2023. [1](#), [2](#), [5](#), [6](#), [4](#)
- [18] Wenchao Ma, Bin Tan, Nan Xue, Tianfu Wu, Xianwei Zheng, and Gui-Song Xia. How-3d: Holistic 3d wireframe perception from a single image. In *Int. Conf. 3D Vis.*, 2022. [2](#)
- [19] David Marr. *Vision: A computational investigation into the human representation and processing of visual information*. MIT press, 2010. [1](#), [2](#)
- [20] Ishit Mehta, Manmohan Chandraker, and Ravi Ramamoorthi. A level set theory for neural implicit evolution under explicit flows. In *European Conference on Computer Vision (ECCV)*, pages 711–729, 2022. [3](#)
- [21] Ben Mildenhall, Pratul P. Srinivasan, Matthew Tancik, Jonathan T. Barron, Ravi Ramamoorthi, and Ren Ng. NeRF: representing scenes as neural radiance fields for view synthesis. In *European Conference on Computer Vision (ECCV)*, pages 405–421, 2020. [3](#)
- [22] Jeong Joon Park, Peter R. Florence, Julian Straub, Richard A. Newcombe, and Steven Lovegrove. DeepSDF: Learning continuous signed distance functions for shape representation. In *IEEE Conf. Comput. Vis. Pattern Recog.*, 2019. [2](#)
- [23] Rémi Pautrat, Juan-Ting Lin, Viktor Larsson, Martin R. Oswald, and Marc Pollefeys. SOLD2: self-supervised occlusion-aware line description and detection. In *IEEE/CVF Conference on Computer Vision and Pattern Recognition (CVPR)*, pages 11368–11378, 2021. [1](#), [2](#)
- [24] Rémi Pautrat, Iago Suárez, Yifan Yu, Marc Pollefeys, and Viktor Larsson. Gluestick: Robust image matching by sticking points and lines together. In *IEEE Conf. Comput. Vis. Pattern Recog.*, 2022. [1](#), [2](#)
- [25] Rémi Pautrat, Daniel Barath, Viktor Larsson, Martin R. Oswald, and Marc Pollefeys. DeepSLD: Line segment detection and refinement with deep image gradients. In *IEEE/CVF Conference on Computer Vision and Pattern Recognition (CVPR)*, 2023. [2](#), [1](#)
- [26] Albert Pumarola, Alexander Vakhtov, Antonio Agudo, Alberto Sanfeliu, and Francesc Moreno-Noguer. PL-SLAM: real-time monocular visual SLAM with points and lines. In *IEEE International Conference on Robotics and Automation (ICRA)*, pages 4503–4508, 2017. [2](#)
- [27] Johann Salaün, Renaud Marlet, and Pascal Monasse. Multiscale line segment detector for robust and accurate sfm.

- In *International Conference on Pattern Recognition (ICPR)*, pages 2000–2005, 2016. [2](#)
- [28] Cordelia Schmid and Andrew Zisserman. Automatic line matching across views. In *IEEE/CVF Conference on Computer Vision and Pattern Recognition (CVPR)*, pages 666–671, 1997. [2](#)
- [29] Johannes L. Schönberger and Jan-Michael Frahm. Structure-from-motion revisited. In *IEEE/CVF Conference on Computer Vision and Pattern Recognition (CVPR)*, pages 4104–4113, 2016. [1](#), [2](#), [4](#), [5](#)
- [30] Johannes L. Schönberger, Enliang Zheng, Jan-Michael Frahm, and Marc Pollefeys. Pixelwise view selection for unstructured multi-view stereo. In *European Conference on Computer Vision (ECCV)*, pages 501–518, 2016. [2](#)
- [31] Kokichi Sugihara. A necessary and sufficient condition for a picture to represent a polyhedral scene. *IEEE Trans. Pattern Anal. Mach. Intell.*, 6(5):578–586, 1984. [2](#)
- [32] Christopher Sweeney, Tobias Höllerer, and Matthew A. Turk. Theia: A fast and scalable structure-from-motion library. In *ACM International Conference on Multimedia (ACMMM)*, pages 693–696, 2015. [2](#)
- [33] Bin Tan, Nan Xue, Song Bai, Tianfu Wu, and Gui-Song Xia. Planetr: Structure-guided transformers for 3d plane recovery. In *Int. Conf. Comput. Vis.*, pages 4166–4175, 2021. [2](#)
- [34] Bin Tan, Nan Xue, Tianfu Wu, and Gui-Song Xia. NOPE-SAC: neural one-plane RANSAC for sparse-view planar 3d reconstruction. *IEEE Trans. Pattern Anal. Mach. Intell.*, 45(12):15233–15248, 2023. [2](#)
- [35] Matthew Tancik, Vincent Casser, Xinchen Yan, Sabeek Pradhan, Ben P. Mildenhall, Pratul P. Srinivasan, Jonathan T. Barron, and Henrik Kretschmar. Block-nerf: Scalable large scene neural view synthesis. In *IEEE Conf. Comput. Vis. Pattern Recog.*, 2022. [8](#)
- [36] Rafael Grompone von Gioi, Jérémie Jakubowicz, Jean-Michel Morel, and Gregory Randall. LSD: A fast line segment detector with a false detection control. *IEEE Trans. Pattern Anal. Mach. Intell.*, 32(4):722–732, 2010. [2](#)
- [37] Bing Wang, Lu Chen, and Bo Yang. Dm-nerf: 3d scene geometry decomposition and manipulation from 2d images. In *International Conference on Learning Representations (ICLR)*, 2023. [3](#)
- [38] Qiuyuan Wang, Zike Yan, Junqiu Wang, Fei Xue, Wei Ma, and Hongbin Zha. Line flow based simultaneous localization and mapping. *IEEE Trans. Robotics*, 37(5):1416–1432, 2021. [2](#)
- [39] Dong Wei, Yi Wan, Yongjun Zhang, Xinyi Liu, Bin Zhang, and Xiqi Wang. ELSR: efficient line segment reconstruction with planes and points guidance. In *IEEE Conf. Comput. Vis. Pattern Recog.*, pages 15786–15794, 2022. [1](#), [2](#)
- [40] Changchang Wu. Towards linear-time incremental structure from motion. In *International Conference on 3D Vision (3DV)*, pages 127–134, 2013. [2](#)
- [41] Qianyi Wu, Xian Liu, Yuedong Chen, Kejie Li, Chuanxia Zheng, Jianfei Cai, and Jianmin Zheng. Object-compositional neural implicit surfaces. In *European Conference on Computer Vision (ECCV)*, pages 197–213, 2022. [3](#)
- [42] Yuxi Xiao, Nan Xue, Tianfu Wu, and Gui-Song Xia. Level- s^2 fm: Structure from motion on neural level set of implicit surfaces. In *IEEE Conf. Comput. Vis. Pattern Recog.*, 2023. [2](#)
- [43] Nan Xue, Song Bai, Fudong Wang, Gui-Song Xia, Tianfu Wu, and Liangpei Zhang. Learning attraction field representation for robust line segment detection. In *IEEE/CVF Conference on Computer Vision and Pattern Recognition (CVPR)*, pages 1595–1603, 2019. [2](#), [1](#)
- [44] Nan Xue, Tianfu Wu, Song Bai, Fudong Wang, Gui-Song Xia, Liangpei Zhang, and Philip H. S. Torr. Holistically-attracted wireframe parsing. In *IEEE/CVF Conference on Computer Vision and Pattern Recognition (CVPR)*, pages 2785–2794, 2020. [1](#), [3](#)
- [45] Nan Xue, Song Bai, Fudong Wang, Gui-Song Xia, Tianfu Wu, Liangpei Zhang, and Philip H. S. Torr. Learning regional attraction for line segment detection. *IEEE Trans. Pattern Anal. Mach. Intell.*, 43(6):1998–2013, 2021.
- [46] Nan Xue, Tianfu Wu, Song Bai, Fu-Dong Wang, Gui-Song Xia, Liangpei Zhang, and Philip H. S. Torr. Holistically-attracted wireframe parsing: From supervised to self-supervised learning. *IEEE Trans. Pattern Anal. Mach. Intell.*, 45(12):14727–14744, 2023. [1](#), [2](#), [3](#), [6](#), [8](#), [5](#)
- [47] Yao Yao, Zixin Luo, Shiwei Li, Jingyang Zhang, Yufan Ren, Lei Zhou, Tian Fang, and Long Quan. Blendedmvs: A large-scale dataset for generalized multi-view stereo networks. In *IEEE/CVF Conference on Computer Vision and Pattern Recognition (CVPR)*, pages 1787–1796, 2020. [2](#), [5](#), [6](#)
- [48] Lior Yariv, Yoni Kasten, Dror Moran, Meirav Galun, Matan Atzmon, Ronen Basri, and Yaron Lipman. Multiview neural surface reconstruction by disentangling geometry and appearance. In *Advances in Neural Information Processing Systems (NeurIPS)*, 2020. [3](#)
- [49] Lior Yariv, Jiatao Gu, Yoni Kasten, and Yaron Lipman. Volume rendering of neural implicit surfaces. In *Advances in Neural Information Processing Systems (NeurIPS)*, 2021. [2](#), [3](#), [5](#), [8](#), [1](#)
- [50] Zehao Yu, Songyou Peng, Michael Niemeyer, Torsten Sattler, and Andreas Geiger. Monosdf: Exploring monocular geometric cues for neural implicit surface reconstruction. In *Advances in Neural Information Processing Systems (NeurIPS)*, 2022. [8](#)
- [51] Yichao Zhou, Haozhi Qi, and Yi Ma. End-to-end wireframe parsing. In *IEEE/CVF International Conference on Computer Vision (ICCV)*, pages 962–971, 2019. [1](#)
- [52] Yichao Zhou, Haozhi Qi, Yuexiang Zhai, Qi Sun, Zhili Chen, Li-Yi Wei, and Yi Ma. Learning to reconstruct 3d manhattan wireframes from a single image. In *IEEE/CVF International Conference on Computer Vision (ICCV)*, pages 7697–7706, 2019. [1](#)